At the Intersection Between Optics and mmWave Design: An Energy Autonomous 5G-Enabled Multilens-Based Broadbeam mmID for "Smart" Digital Twins Applications

Charles A. Lynch, III, *Student Member, IEEE*, Genaro Soto-Valle, *Graduate Student Member, IEEE*, Jimmy G. D. Hester, and Manos M. Tentzeris, *Fellow, IEEE*

***Abstract*— For the first time, the authors propose a 5G/mmWave multilens-based retrodirective backscatter system capable of large coverage in both azimuth and elevation directions. The structure features two biconvex lenses backed by an array of individual backscattering elements (pixels). The components of the system are described in detail, including the cascaded polytetrafluoroethylene (PTFE) lenses and the pixel array. Subsequently, the entire system is assembled, and its detectability and large azimuth/elevation coverage is measured and compared to the state-of-the-art. The millimeter wave identification (mmID) displays a peak differential radar cross section (RCS) of −15.7 dBsm with a −10 dB coverage of 2.244 sr about boresight, improving the angular coverage by over 204%, relative to a single-lens-based mmID. A theoretical link budget analysis is presented for the best- and worst case incidence angles. Using the maximum allotted 75 dBm equivalent isotropic radiated power (EIRP) in 5G/mmWave frequencies, reading ranges of 5.88 and 3.35 km are envisioned with incidence angles of 0° and 50°, respectively. To demonstrate its long-range potential for localized sensing applications, a proof-of-concept (PoC) frequency modulated continuous wave (FMCW) radar is used to range the multi-lens mmID up to 82.5 m within 6 cm of the true range even at the worst case incidence angle. This approach could potentially unlock the deployment of dense battery-less 5G-connected localizable mmID the Internet-of-Things (IoT) swarms in "Smart" digital twinning applications.**

***Index Terms*— Broad-angular coverage, digital twins, energy autonomous, 5G, Internet-of-Things (IoT) swarm, localization, millimeter wave identification (mmID), millimeter wave (mmWave) lenses, smart cities, smart manufacturing.**

I. Introduction

With numerous recent developments and deployments of 5G/mmWave and radar technologies, unique opportunities to form battery-free ubiquitous sensing systems to provide real-time sensor-driven optimized the Internet-of-Things (IoT) swarms serviced by the 5G infrastructure and autonomous vehicles have arisen. There are several challenges when it comes to the realization of wireless sensor swarms namely: the large path loss incurred due to the high frequency of operation, the need to power each wireless sensor node in these swarms in some fashion, and the ability to accurately locate each sensor. By addressing all three challenges, a highly scalable, energy autonomous, 5G/mmWave IoT swarm can be formed. By deploying these IoT swarms in buildings, factories, or entire cities and wireless collecting the sensor and localization information from each node, digital twinning—a digital presentation of a system—for the monitoring and optimal operation of each environment can be formed. Through leveraging the aforementioned deployed 5G/mmWave base stations as the wireless centers for collecting and forming these digital twins of the environment, a complete cyberphysical system (CPS), a cyber model created from sensor input from the physical environment, is formed. Furthermore, to realize this massive scale of sensors throughout a physical area, the sensors themselves need to operate energy autonomously. By removing the need of batteries to form and operate these digital twinning systems, a massive reduction in the maintenance and environmental costs of constantly replacing the batteries can be achieved and with it the realization of such 5G-enabled "Smart" systems.

One such method to overcome the path loss issue is by having directive wireless sensor nodes that can focus their signals back to a 5G base-station. This has been achieved with the use of phased-array-based architectures. Zhang et al. [1] presented a Ku-band 1-bit reflectarray-based magnetoelectric (ME) dipoles for a high-gain, wide-band operation for steering the reflected electromagnetic energy. While this design is passive, the design is static and only provides one steering angle, making it ill-suited for deploying throughout a complex environment. Dai et al. [2] presented a 256 element 2-bit reconfigurable beamforming array constructed of positive-intrinsic-negative (p-i-n) diodes. While the system presented a gain of 19 dBi with scanning angles of ±60°, the power consumption of the system was 153 W. Thus, this technology would not allow for energy autonomous operation. Thus,

Manuscript received 14 July 2023; revised 13 September 2023; accepted 13 October 2023. Date of publication 3 January 2024; date of current version 4 April 2024. This work was supported by NSF. This article is an expanded version from the International Microwave Symposium, San Diego, June 15 2023. *(Corresponding author: Charles A. Lynch, III.)*

Charles A. Lynch, III, Genaro Soto-Valle, and Manos M. Tentzeris are with the Department of Electrical and Computer Engineering, Georgia Institute of Technology, Atlanta, GA 30332 USA (e-mail: clynch19@gatech.edu).

Jimmy G. D. Hester is with Atheraxon Inc., Atlanta, GA 30332 USA.

Color versions of one or more figures in this article are available at https://doi.org/10.1109/TMTT.2023.3344538.

Digital Object Identifier 10.1109/TMTT.2023.3344538

5G/mmWave IoT systems for digital twinning that are solely based on phased array-based technologies for sensor nodes make the environmental and maintenance costs of constantly replacing the batteries of these sensor nodes prohibitive for the realization of these IoT swarms.

A technology that allows for highly scalable sensor nodes with continuous ultralow-power consumption, enabling the removal of batteries—thereby reducing the environmental and maintenance costs of these 5G IoT swarms—is backscatter communication. In this form of communication, the sensor nodes are able to encode sensor information on the interrogator signal from a 5G base-station by modulating the radar cross section (RCS) of the transponder. This signal with the encoded sensor information is reflected back to the base station to be processed for optimal operation of the CPS being monitored. However, despite the highly energy efficient communication scheme, to provide a highly reconfigurable, steerable backscattering node, the design would require phase shifters and power-hungry logic circuits. This would increase the power consumption and complexity of the design impeding the usage of backscattering communication for these IoT swarms. Fortunately, various works that break the high gain and angular coverage trade-off have been recently reported, effectively eliminating the need of the a priori knowledge of the location of the interrogator, through the use of semi-passive and passive retro-directive millimeter wave identification (mmID) structures. One such structure is a Van-Atta array, a retrodirective structure based on re-transmission in the angle of arrival by connecting antenna elements together with equal electrically long transmission lines was first presented in [3]. Hester and Tentzeris [4] presented a chipless 5G/mmWave cross-polarized Van-Atta array designed on Kapton for local humidity sensing and was detected at 30 m from a proof-of-concept (PoC) reader. This base design was then integrated into a semi-passive topology with an ultralow-power transistor (NE3520S03) for ultra-long-range applications and energy autonomous operation of local ammonia sensing with the mmID interrogated from 80 m away from a PoC reader [5]. While these designs displayed long-range operation, there is a fundamental limit of detectability of these designs due to the lack of "RF combining" over the aperture of the mmIDs. Structures that operate on this "RF combining" principle are lens-based structures which focus incoming electromagnetic energy to a designed focal distance from the lens. By focusing the electromagnetic energy, these mmIDs are able to achieve higher detectability while exhibiting retrodirective behavior. Eid at al. [6] presented a 28 GHz Rotman lens-based semi-passive mmID with high detectability over wide angular ranges and detected the mmID at 64 m away from a PoC reader. With the use of a solar cell and an ultralow-power baseband circuit for frequency modulation, the device operated completely energy autonomous. Along with this semi-passive mmID, a harmonic dual Rotman lens-based mmID was first presented in [7]. By cascading two Rotman lenses, connected with a fully passive doubler circuit, the device was detected 65 m away from a reader. The authors expanded this fully passive design to a localization application and was ranged with sub-mm accuracy 10 m away from a PoC harmonic radar scheme [8]. While these mmIDs promise highly detectable backscattering responses over a wide-angle coverage, all these previous mmIDs only exhibit retrodirective behavior over only one plane—typically azimuth is chosen—and would lose coverage rather drastically when considering differences in elevation. This problem is critical in typical urban environments and autonomous areas for "Smart" manufacturing where mmIDs and their 5G base stations can easily be placed at very different elevations and present quite oblique angles to each other. These also tend to be the wireless setups where the highest densities of such devices are likely to be installed for the creation of digital twinning systems.

In terms of localization, these mmIDs need to be interrogated with accurate positional information in a highly affordable way. This positional information of the mmIDs is heavily important with respect to a CPS formed from IoT swarms as with this spatial information, a more detailed model of the CPS can be formed. A wireless interrogation scheme that has shown great promise in both cost and accuracy is the frequency-modulated continuous wave (FMCW) radar. With the recent developments of 5G/mmWave radio frequency integrated circuits (RFICs) technology, these FMCW radars have become commodities and have been widely deployed in commercial products from autonomous driving [9] to "Smart" home products [10]. Various works have already proposed the usage of FMCW radars and backscattering transponders at 5G/mmWave and have demonstrated a high localization accuracy using either 24 GHz [11] and 60 GHz [12] wireless bands for close range accuracy. Additionally, due to the mmIDs backscattering response, the mmIDs are able to modulate away from the static clutter and self-interference of the transmitting antenna operating on the same frequency channel, making this form of wireless interrogation highly suitable for the localized sensing used in IoT swarms.

Therefore, in an effort to address the lack of fully hemispherical solid angular coverage for localized sensing applications, the authors propose a highly accurate ranging system of a multilens-based mmID. Lynch et al. [13] presented the first-ever 3-D-lens-based mmID providing retrodirective behavior in both azimuth and elevation. The work presented here builds on this effort by extending the number of lens elements to two to achieve both higher detectability and as well as improved solid angular coverage. Additionally, the authors present a design method taking into account the optical concept of ray-tracing and 5G/mmWave antenna design. Furthermore, the multilens-based mmID operates completely energy autonomously and is easily detected and ranged accurately in long-range scenarios under best and worst case conditions of boresight and 50° angle of incidence. Thus, the proposed system presents a highly scalable, energy autonomous 5G/mmWave framework to create future IoT swarms for localized sensing in CPSs deployed in highly complex "Smart" city environments. The remaining sections of the article are structured as follows: Section II presents the design and characterization of the proposed multilens-based mmID. Section III presents a theoretical link budget analysis of the current PoC FMCW radar and a future system utilizing 75 dBm equivalent isotropic radiated power (EIRP),

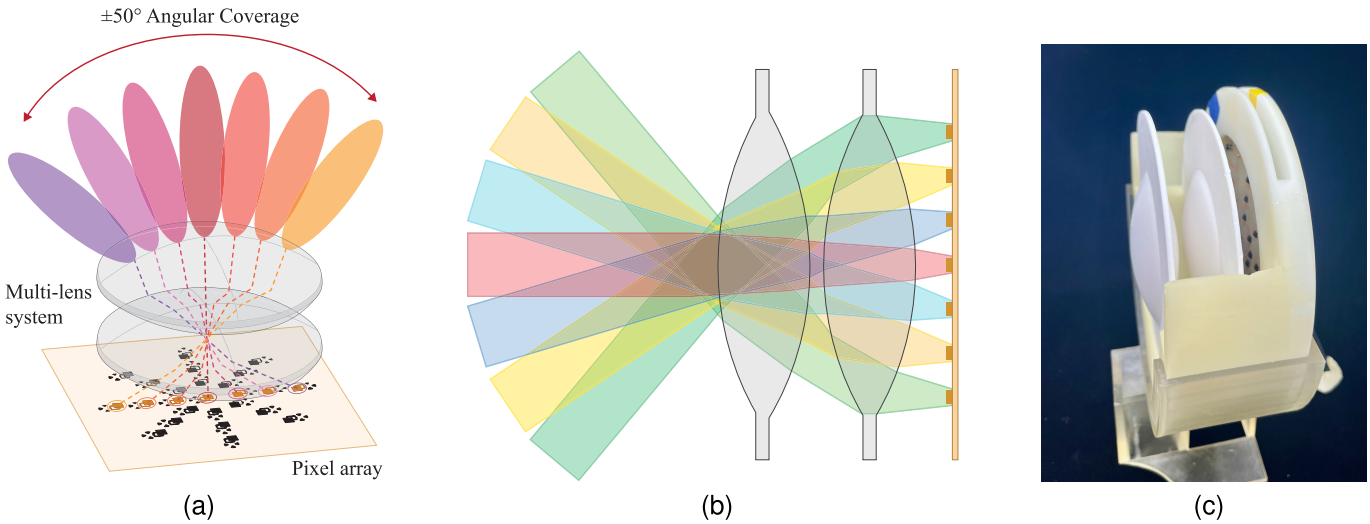

Fig. 1. (a) Diagram of the horizontal axis of coverage enabled by the multilens-based mmID. (b) Cross-sectional view of the multilens-based mmID; similar spherically symmetrical coverage can be achieved in vertical, diagonal, and arbitrary orientation axis. (c) Fabricated PoC energy autonomous multilens-based mmID for the realization of IoT swarms.

the maximum allotted EIRP in 5G/mmWave bands dictated by the Federal Communications Commission (FCC). Section IV describes the assembled PoC FMCW radar and a demonstration of highly accurate ranging the multilens-based mmID at best and worst case scenarios of angles of incidence of the mmID is presented. Finally, in Section V, conclusions are drawn from the presented results along with remarks on the future work of the proposed system.

II. Proposed 5G-Enabled Energy Autonomous 3-D Lens-Based mmIDs

As aforementioned, to provide the sustainable and scalable 5G/mmWave IoT swarm infrastructure, the camera-inspired 3-D lens-based mmID was proposed in [13]. The design considerations for this mmID were centered around maintaining high detectability over a wide-angular coverage in both vertical and horizontal axes. This was achieved with a single meniscus elliptical lens with a peak differential RCS of -26.5 dBsm with an angular coverage of ± 28 °C of angular coverage over two-axes. This was the first-ever demonstration of a retrodirective 3-D lens-based mmID. However, although the previously reported design improves on the solid angular coverage compared to that of Van-Atta array and Rotman lens configurations, the angular coverage of the 3-D lens-based mmID still has much to be desired. However, using a multi-lens system, similar to the concept of a wide-camera lens, typically made up of several lens elements to correct for off-axis aberrations, the mmID expands its angular coverage to $\pm 50°$ over two axes while simultaneously improving the detectability of the mmID with multiple stages of focusing. Therefore, to achieve this the authors present a multilens-based mmID formed from two 5G/mmWave lenses and a similar backscattering pixel arary. Schematics highlighting both horizontal and vertical cuts are displayed in Fig. 1(a) and (b) with the fabricated PoC prototype presented in Fig. 1(c). Additionally, the semi-passive mmID has an integrated ultralow-power baseband circuit, enabling energy autonomous operation for ultra-long ranging of the mmIDs in complex urban environments for the creation of digital twinning wireless infrastructure.

A. 5G/mmWave Multi-Lens Design

A topology of a cascaded 3-D lens is a natural solution for higher detectability with more stages of magnification and increased angular view as seen in typical wide-view camera lens systems. However unlike traditional commercially available wide-view camera lens systems operating at optical frequencies which can have as many as ten different lenses cascaded together, the height of such 5G/mmWave lens system would be rather large compared to the previous single lens design (as much as $4\times$). Therefore, we propose a minimalist cascaded lens system with only two stages of bi-convex lenses. To guide the design procedure of the multi-lens system the equation of the angular-field-of-view (AOF) described as

$$\text{AOF} = 2\arctan\left(\frac{h}{2F}\right) \tag{1}$$

where h is the height of the receiving RF "pixel" array and F is the equivalent focal length of the multi-lens system. Therefore, by increasing the height of the RF "pixel" array and reducing the focal length of the cascaded lens system, the multilens-based mmID can achieve a wider angular coverage. By setting the height of the receiving array to be 57 mm and setting a minimum angular coverage of 104°, the focal length is calculated to be 22 mm. Having established the focal length of the system, using Optometrika, a ray tracing lens system design software MATLAB suite, and numerous simulations were performed stepping the sensor array from the back surface of the second lens for varying radii of curvature. To determine the focal length of the cascaded lenses, the bundle focus standard deviation in mm, or spread of the ray bundle, was recorded at each working distance. With a minimum indicating the effective focal length of the multi-lens system and the target being the 22 mm focal length. The final

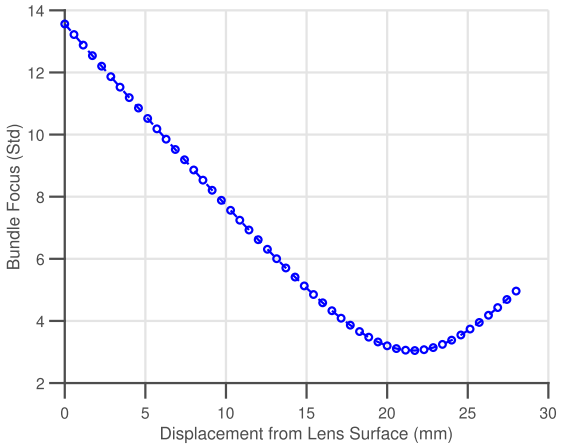

Fig. 2. Standard deviation of the ray bundle at each working distance from the back surface of the second lens with 0° angle of incidence.

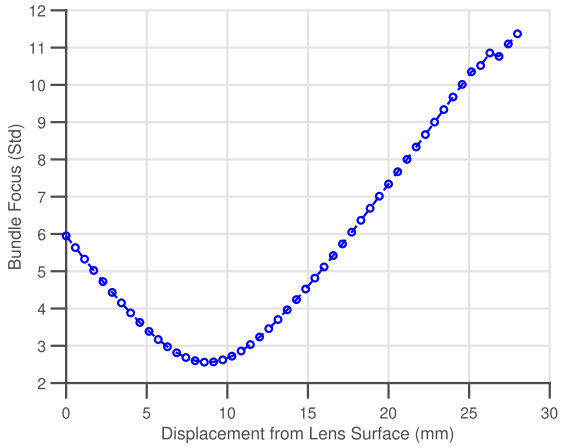

Fig. 3. Standard deviation of the ray bundle at each working distance from the back surface of the second lens with 50° angle of incidence (outermost off-axis "pixel" element).

radii of curvature selected of the cascaded lens system was 70 and −75 mm for the first stage bi-convex lens and 68 and −68 mm for the second bi-convex lens. The standard deviation of this ray bundle that intersected the sensor was recorded at each distance in the simulation tool and is displayed in Fig. 2 confirming that the cascaded lenses provide the desired focal depth from the back surface at boresight. When considering a single lens system with an equivalent focal distance, the maximum diameter, thereby aperture size of the dielectric lens, will be limited and result in lower detectability while providing similar angular coverage. When considering the off-axis elements in the planar RF "pixel" array, with the outermost element displaced by 28.5 mm from the center of the lenses equaling one half of the total height h of the RF "pixel" array of the multi-lens system—as will be discussed in Section II-B. The outermost element would then have a total radial distance of 36 mm from the back of the second lens. This would result in a de-focusing of the electromagnetic energy that impinges onto the outermost element leading to a reduced angular coverage. A simple solution to overcome this displacement is to decrease the working distance of the RF "pixel" array from the back surface of the multi-lens system. Thus a similar sweep in the working distance of the sensor in the Optometrika software was done with the cascaded lens system with an angle of incidence of 50° and is presented in Fig. 3. From these results, the optimal working distance to provide adequate focusing of the incoming electromagnetic energy at the angular edge of operation is 8 mm from the back surface of the second lens. This comes with an expected trade-off of a slight de-focusing corresponding to a reduction in the peak gain of the mmID itself of the center elements in the pixel array.

Having established the lens design from the optical software suite, the same two lenses were then constructed in CST microwave suite and simulated with the updated "pixel" array. Polytetrafluoroethylene (PTFE) ($\epsilon_r = 2.1$ and $\tan\delta = 0.001$) a low-loss dielectric material was selected as the lenses material to reduce dielectric losses that would be incurred as the incoming electromagnetic energy is focused through the lens system. This is crucial as this dielectric loss penalizes the RCS of the mmID twice due to the receive and reflecting nature of the backscatter communication. A sweep of diameter was then conducted to survey the optimal diameter of the cascaded lens system similar to the diameter study shown in [13]. The diameter for these simulations was swept from 28 to 84 mm in steps of 4 mm and the results from this simulation study are shown in Fig. 4. The simulation results exhibit an expected trend of increasing peak realized gain of the multi-lens system with an increase in lens system diameter. The non-monotonic behavior observed in the realized gain is due to shifting the optimal focus from the inner elements to outer elements. The angular coverage displays periodic local maxima due to outer elements in the pixel array coming in and out of focus. The absolute value of the angular coverage at each local maximum decreases with an increase in the diameter of the lens system. With the goal of the mmID to have improved gain and a minimum angular coverage greater than 100°, the optimal diameter from this sweep was a diameter of 68 mm. Therefore, the multi-lens system, designed and optimized with optical and EM simulation tools, enables a highly detectable mmID over wide angular ranges even at highly oblique angles of 50° off boresight and allows for the framework for orientation-agnostic wireless sensor nodes suitable for the creation of digital twinning infrastructure to be deployed in "Smart" urban and manufacturing environments.

B. Energy Autonomous RF "Pixel" Array Design

The design of the RF "Pixel" array for the multi-lens mmID was similar to that of the single lens design. Each element consists of a cross-polarized 28 GHz square patch antenna, a multiple of ($\lambda/2$) microstrip transmission line to match the input impedance of each feeding edge of the patch antennas, and a low-cost FET-based (CE3520K3 from CEL) switch; its dimension can be seen in the inset of Fig. 5. The switch further comprises radial stubs and a connection to the switched line, with appropriate dimensions to effectively switch the length of the parallel stub from ($\lambda/4$) to ($\lambda/2$). Thus allowing for amplitude-based sub-carrier generation on the received signal from a reader. Finally, two isolating 28 GHz

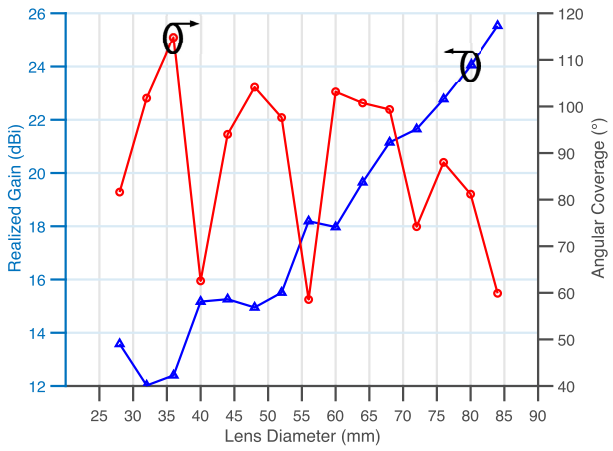

Fig. 4. Simulation results for the peak realized gain and 3 dB angular coverage as a function of the diameter of the PTFE multi-lens system.

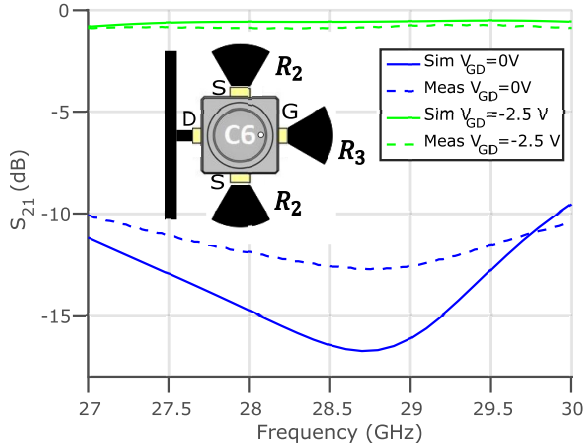

Fig. 5. Measured S_{21} of the biased and unbiased states of the ultralow-power FET-based switch and single element schematic (inset) with drain, gate, and source pins along with $R_2 = 1.14$ mm, and $R_3 = 1.55$ mm labeled.

$s\frac{\lambda}{4}$ radial-stub-based RF chokes, enabling baseband biasing between the gate and drain of the FET, were added. The backscattering element was designed on a Rogers CLTE-MW ($\epsilon_r = 3.03$, $\tan\delta = 0.0015$) with a thickness of 0.254 mm. The FET switch was characterized for both biased and unbiased conditions, displaying more than 11 dB attenuation between its two states, as shown in the insertion loss Fig. 5. Under biasing conditions, this ultralow-cost switch consumes less than 1 μW while providing close-to-ideal properties for the modulation of the backscattered signal. With this power consumption, harvesting energy from the environment can be easily achieved to provide an energy autonomous semi-passive mmID to be used in digital twinning wireless architectures.

The backscattering element was then arrayed in three concentric circles of 19, 38, and 57 mm in diameter—each with eight patches distributed around each circle and a single element in the center, as displayed in Fig. 6. The inter-element spacing of 9.5 mm (0.88λ at 28 GHz) was chosen as this was the minimum spacing required to allow the placement of the connecting transmission lines, RF front-end, and biasing lines on the same layer. Furthermore, the connecting transmission lines were connected to either the left and bottom edges of the square patch element or right and top edges, thereby, keeping all pixel elements in-phase with each other to prevent any cancellation of the re-transmitted backscattering signal. Additionally, this placement allowed for the ease of routing of baseband V_{bias} connections on the same plane. With each individual element beamwidth through the multi-lens being 14.28°, the proposed topology provides the desired ±50°, due to splitting up the total 100° of coverage of the top hemisphere by seven elements. Assuming each element maintains the same peak gain and beamwidth through the lens system, a relationship between angular coverage can be expressed as $14.28(2n + 1)$ with n being the number of concentric circles. Additionally, by adding concentric circles, a similar lens optimization for diameter sweep would need to be made to select the optimal angular coverage and realized gain of a future multilens-based mmID. In addition to the RF front-end design, a baseband circuit to generate the modulation frequency of the backscattering array was assembled with commercially off the shelf (COTS) components. The baseband is made up from an ultralow-power linear voltage regulator XC6504A301MR-G, a resistance-based voltage-controlled oscillator (VCO) LTC6906, and two parallel MP3-25 flexible solar cells used to power the entire backscattering array. The voltage regulator provides a stable supply voltage from the flexible solar cell that is fed into the VCO. It has to be stressed that the regulator and VCO are essential to the ranging extraction. As explained in Section IV-A, the ranging information extracted by FMCW systems is linearly dependent on frequency peaks measured in the baseband spectrum. Therefore, with unstable voltages and oscillation frequencies, jitter could greatly degrade the accuracy of the ranging information. Additionally, the resistance-based VCO enables frequency division multiplexing (FDM), where each tag's modulation frequency can be used as a unique "ID," thereby providing a framework to build the envisioned energy autonomous IoT swarm for digital twinning applications with the ability to simultaneously localize multiple tags in the field-of-view (Fov) of the PoC radar. The number of mmIDs that a given FMCW radar can support is restricted by the sampling rate of the baseband received signal and the maximum reading range each interrogator system can support. This spectral usage is based on the maximum spread of the two modulation frequency components centered about the modulation frequency of each mmID due to ranging information described in Section IV. Restricting the maximum distance of the proposed IoT swarm to a 95 m radius—well within the maximum reading range of the proposed mmID described in Section III—from the interrogator, a total baseband spectral usage of 126.66 kHz per tag is calculated. With a baseband sample rate of 2 MHz of the PoC FMCW radar, the total number of mmIDs that can be localized simultaneously can be estimated a priori. The set resistor was set to a value of 122 kΩ resulting in a modulation frequency of 817 kHz based on the data sheet of the LTC6906.

The power consumption of the entire RF "pixel" array was measured to be 450 μW with a stable 3 V supply from the flexible solar cell (V_s in Fig. 6). The power consumption needs to be considered when designing for a large angular coverage

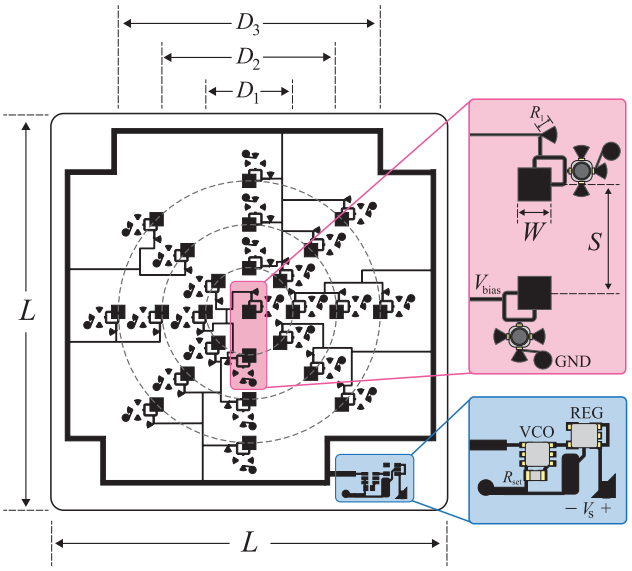

Fig. 6. Energy autonomous 28 GHz cross-polarized mm-Wave backscattering elements ("pixels") layout for "composite" mmIDs including the single "pixel" and baseband circuitry highlighted with dimensions labeled $L = 60$ mm, $D_1 = 19$ mm, $D_2 = 38$ mm, $D_3 = 57$ mm, $W = 2.9$ mm, $S = 9.5$ mm, and $R_1 = 1.22$ mm.

of the multi-lens mmID as well as with each additional circle of elements an additional eight elements are added and would therefore increase the power consumption by 144 μW per concentric circle. Thus, the proposed RF "pixel" array allows for energy autonomous operation in both indoor (with indoor lighting conditions) and outdoor environments for the realization of scalable "Smart" cities, "Smart" manufacturing environments, and digital twinning wireless infrastructure.

C. Angular Coverage Characterization of Mulit-Lens-Based mmID

Having designed and characterized the 5G/mmWave lenses and the backscattering array, the two subsystems were assembled together to form the proposed multilens-based mmID and its differential RCS and angular coverage were measured. The mmID was placed at 1.4 m from two co-located cross-polarized wide-band horn antennas. The mmID was then precisely rotated from $-90°$ to $90°$ in steps of $5°$ and the unbiased and biased states were measured at each of these angular steps. The measurement was then repeated for horizontal, vertical, and $-45°$ cuts. Then the differential RCS, or the detectability of the mmID, was calculated using the expression

$$\Delta\sigma_{\mathrm{RCS}} = \frac{\lambda^2 G_{\mathrm{mmID}}{}^2 |\Gamma_A - \Gamma_B|^2}{4\pi} \tag{2}$$

where λ, G_{mmID}, Γ_A, and Γ_B are the wavelength of operation in meters, the gain of the mmID, and the reflection coefficients of the front-end in biased and unbiased states, respectively. A 6-in-radius metal sphere was used as a reference target, for the accurate normalization of the RCS measurements. The results of this described differential RCS and simulated differential RCS are displayed in Fig. 7. The results display good agreement between measured and simulated differential

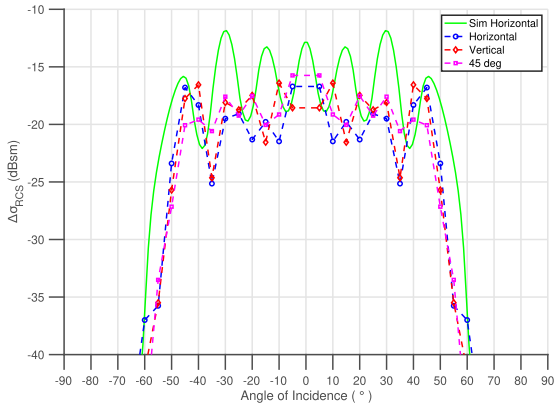

Fig. 7. Simulated and measured differential RCS of the multilens-based mmID for horizontal, vertical, 45° angular cuts.

RCS of the mmID with the multi-lens mmID displaying a peak measured differential RCS of -15.7 dBsm with a -10 dB angular coverage of $\pm 50°$ across all cuts. The total operational bandwidth proposed of the mmID is approximately 620 MHz centered around 28.3 GHz. Three metrics were used to evaluate and compare the proposed system (shown in Table I) to other reflectarray-based and lens-based mmIDs of the literature: the peak differential RCS, the azimuth and elevation angular coverage, and the total solid angle of coverage. When comparing to the previous single lens design presented in [13], the multi-lens mmID displays a higher detectability with an increase by more than 10 dB to the peak differential RCS while improving the solid angle by over 204%. When comparing to the dual Rotman lens harmonic-based mmID presented in [8], the proposed mmID displays a higher detectability more than 20 dB, due to the conversion loss of generating the harmonic backscatter signal, while improving the solid angular coverage by over 393%. When comparing to the Van-Atta counter part presented in [5], the multilens-based mmID displays an expected superior detectability along with an improvement to the angular coverage by over 310%. This is due to nature of the RF combining taking place with the lens-based architecture compared to the Van-Atta which operates on the principle of RF division and re-transmission. When comparing to the semi-passive Rotman lens-based mmID presented in [6], the proposed mmID presents a similar detectability while further improving the solid angular coverage by over 310%. Therefore, when considering the complex urban and "Smart" manufacturing environments where these mmIDs will be deployed, the proposed mmID displays a rather orientation-agnostic behavior up to angles of 50° of incidence relative to a potential interrogator.

III. Link Budget of 3-D Lens-Based mmIDs

Having characterized the energy autonomous multilens-based mmID in terms of detectability and angular coverage, an analysis of the link budget will now be presented. Four scenarios were considered for the analysis. The first two scenarios are using the PoC FMCW radar described in Section IV as the interrogator with an EIRP of 36 dBm with the multilens-based mmID placed at angles 0° and 50°, the

TABLE I
COMPARISON OF LONG-RANGE REFLECTARRAY AND LENS-BASED RFID/MMID SYSTEMS

Ref.	Freq.	$\Delta\sigma_{RCS}$	Azim./Elev. Coverage	Solid Angle
[8]	14/28 GHz	−35.8 dBsm	±50 °/±7.5 °	0.455 sr
[6]	28 GHz	−15.4 dBsm	±60 °/±7.5 °	0.546 sr
[5]	28 GHz	−29 dBsm	±60 °/±7.5 °	0.546 sr
[13]	28 GHz	−26.5 dBsm	±28 °/±28 °	0.736 sr
This Work	28 GHz	−15.7 dBsm	±50 °/±50 °	2.244 sr

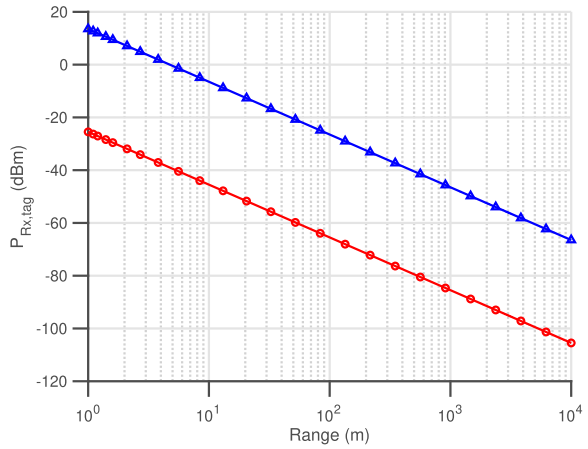

Fig. 8. Power impinging on the multi-lens mmID with EIRP of 36 and 75 dBm.

angular limit of the proposed mmID for the sensitivity of the current PoC reader. The final two scenarios consist of the same setups, but with the maximum allowed EIRP of 75 dBm in 5G/mm-Wave bands to demonstrate the ultra-long-range operation of the ranging system. Two propagation paths were considered for this link budget analysis, namely the link from the interrogator to the multilens-based mmID and the return link back to the interrogator. The power received at the mmID in dB-scale is described by

$$P_{Rx,\text{tag}} = P_{Tx} + G_{Tx} + 10n_{f_o}\log_{10}\left(\frac{\lambda_{f_o}}{4\pi R}\right) \tag{3}$$

where P_{Tx}, G_{Tx}, n_{f_o}, λ_{f_o}, and R are the transmitting power of the FMCW radar in dBm, the gain of the transmitting antenna of the radar in dBi, the path loss exponent of the environment at the fundamental frequency of interrogation which is unitless and depending on the channel conditions of the wireless link, the wavelength of the frequency of operation in meters, and the distance of the mmID from the radar in meters, respectively. This incident power impinging on the mmID versus range is displayed in Fig. 8 with traces of the current 36 and 75 dBm EIRP conditions.

Using the differential RCS, or detectability, of the cascaded 3-D lens-based mmIDs characterized in Section II-C, the return link received power at the reader in dB-scale is described by

$$P_{Rx,\text{Reader}} = G_{Rx} + \Delta\sigma_{\text{RCS}}(\theta,\phi) + 10n_{f_o}\log_{10}\left(\frac{\lambda_{f_o}}{4\pi R}\right) + G_{\text{LNA}} \tag{4}$$

where G_{Rx}, $\Delta\sigma_{\text{RCS}}$, θ, ϕ, n_{f_o}, λ_{f_o}, and G_{LNA} are the gain of the receiving antenna of the radar in dBi, the differential RCS of the mmID in dBsm as a function of azimuth and elevation incidence angles, the azimuth incidence angle of the mmID in degrees, the elevation incidence angle of the mmID in degrees, the path loss exponent of the environment at the operational frequency which is unitless and depends on the channel conditions of the wireless link, the wavelength of the operational frequency in meters, and the gain of the LNA in dB, respectively. The PoC reader sensitivity for this system is based on the PoC sample rate and the number of points in the range fast Fourier transform (FFT) of the PoC FMCW radar. By assuming that the system samples every chirp, the effective sampling rate is then 20 Hz and the sensitivity of the reader in dB-scale is described by

$$S_{Rx} = -173.8 + G_{\text{LNA}} + \text{NF} + 10\log_{10}(F_{\text{Samp}}) + L_{Rx} + M \tag{5}$$

where G_{LNA}, NF, F_{Samp}, L_{Rx}, and M, are the gain of the LNA in dBm, noise figure of the LNA in dB, effective sample rate in Hz, the losses in the cables on the receive channel in dB, and the link margin in dB. With a $M = 6$ and $L_{Rx} = 8$, based on the PoC reader, the sensitivity of the reader was calculated to be −100.79 dBm. The plot of the received power with the current EIRP of the PoC interrogator (36 dBm) and the PoC with the same sensitivity and an EIRP 75 dBm is displayed in Fig. 9, respectively. The maximum reading range of 611 and 337 m of the multi-lens angled at boresight and at 50° with the current PoC demonstrate the ability of the multilens-based mmID to be detected at ultra-long ranges over a wide angular view in both azimuth and elevation angles. When considering the same link with increased transmitting power to equal the maximum allotted EIRP of 75 dBm and maintaining the same sensitivity, the multi-lens mmID features theoretical maximum detectable reading ranges of 5.88 and 3.35 km for boresight and maximum angle interrogation of 50°. Thus, demonstrating the massive potential for ultra-long-range interrogation with a highly robust resilience to the orientation of the proposed multi-lens mmID for the creation of digital twinning systems for future "Smart" city and Smart manufacturing environments.

IV. INTERROGATION OF A POC MULTILENS-BASED MMID PROTOTYPE

A PoC FMCW reader was assembled to demonstrate the ultra-long range and highly accurate ranging of the multilens-based mmID. The PoC reader can be broken down into a transmitting and receiving chain with a block diagram of the PoC displayed in Fig. 10. The transmitter chain of the FMCW radar consists of an 836640L signal generator which produces the FMCW signal which can be expressed in the

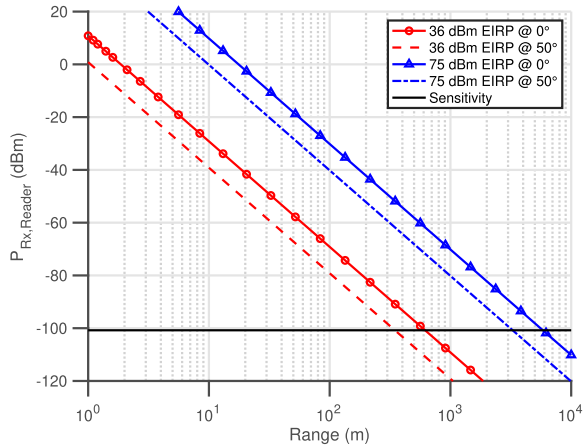

Fig. 9. Received power of the multi-lens mmID at the PoC reader with EIRP of 36 and 75 dBm.

time domain as

$$s_{Tx}(t) = A\cos\left(2\pi\left(f_c t + \frac{B}{T_c}t^2\right) + \phi_o\right) \tag{6}$$

where A, f_c, B, T_c, and ϕ_o are the amplitude of the signal in V, the carrier frequency of the transmitted signal in Hz, the bandwidth of the FMCW chirp signal in Hz, the chirp periodicity in s, and the initial phase of transmitted waveform in radians, respectively. This signal passes through a PS2-53-450/15S power divider to split the FMCW signal into the transmitting or receiving chain. For the remainder of the transmitting chain, this power divided FMCW signal goes through a 26 dB power amplifier to amplify the transmitting signal for long-range interrogation. Afterward, the 28.3 GHz FMCW signal is transmitted by a wide-band 20 dBi gain horn antenna, resulting in an EIRP of 36 dBm, to the mmID in the Fov of the radar. The transmitted signal then travels to the energy-autonomous multilens-based mmID which applies sub-carrier modulation onto the FMCW chirp signal focalized back to the PoC FMCW radar. The mmID signal is then received by an identical 20 dBi horn antenna, configured in the cross-polarized orientation to reduce the self-interference of the transmitting horn, in the form of a delayed FMCW signal with the mmID modulation. The signal is amplified by a RLNA26G40GB 43 dB LNA to limit the noise floor (NF) of the receiver. Afterward, the signal passes through a ALN3325-41-2235 to increase the swing of the received signal and is down mixed with a ADC2640-1 mixer to produce the baseband intermediate frequency (IF) signal. The local oscillator (LO) of the mixer consists of the second part of the power divided FMCW signal from the signal generator. The output of the mixer passes through a baseband lowpass filter to isolate the range spectrum from any high frequency components that are produced by the mixer. Due to the nature of FMCW interrogation, mixing the delayed version of the transmitted signal with the mmID modulation with the original transmitted signal leads to a single frequency tone whose frequency is linearly proportional to two times the round-trip delay time. This resulting time-domain signal then goes through an oscilloscope for sampling and the IF signal

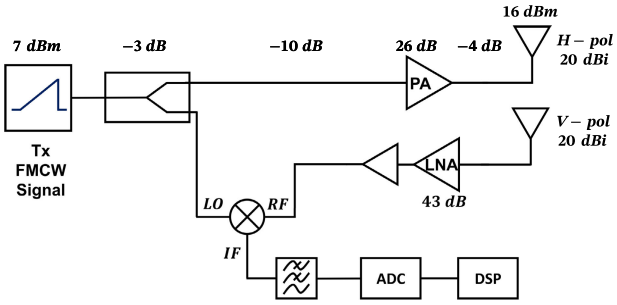

Fig. 10. System block diagram of the PoC FMCW radar for the interrogation of the proposed mmID.

TABLE II
CHIRP PARAMETERS POC FMCW RADAR

Parameter	Value
Frequency Range	27.8-28.8GHz
Bandwidth	1 GHz
Slope	100 MHz ks^{-1}
Sampling Rate	2 MHz
Chirp Periodicity	50 ms
Duty Cycle	20%

over a single chirp period is expressed by

$$s_{Rx}(t) = \frac{\alpha}{2}\cos(2\pi((f_{\text{Mod}} + f_b)t) + \phi_{\text{tot}}) + \frac{\alpha}{2}\cos(2\pi((f_{\text{Mod}} - f_b)t) + \phi_{\text{tot}}) \tag{7}$$

where α, f_{Mod}, f_b, and ϕ_{tot} are the amplitude of the mmID response in V, the modulation frequency of the mmID in Hz, the beat frequency due to the round-trip time delay of propagationHz, and the phase due to the two-way propagation combined with the random modulating phase of the mmID baseband oscillator. The chirp parameters of the PoC 28 GHz FMCW radar are displayed in Table II. These parameters dictate the limitations of the FMCW radar with the main considerations being the maximum range that is limited by the IF sampling rate and the range resolution which is governed by the bandwidth of the chirp signal. The received IF signal, sampled on an oscilloscope, is post-processed in MATLAB for ranging estimations of the multi-lens mmID.

A. Benchmarking of Ranging of Multilens-Based mmID

To evaluate the long-range capabilities of the proposed system, the multilens-based mmID was directly aligned with the reader at boresight to provide the maximum differential RCS. The mmID was then ranged from 2.5 to 82.5 m in steps of approximately 2.5 m. The experimental setup of the PoC FMCW radar and mmID at a maximum range of 82.5 m as shown in Fig. 11. Based on the sweeping bandwidth of the frequency equaling 1 GHz, the range resolution of the FMCW radar is 15 cm. At each range, 50 received IF signals were recorded on the oscilloscope and a FFT of each received IF signal with FFT length of 2^{19} was applied. An example of one range-FFT magnitude spectrum with the multilens-based mmID placed 40 m from the PoC FMCW radar is displayed in Fig. 12. The tag response is highlighted and displays the expected higher and lower frequency components

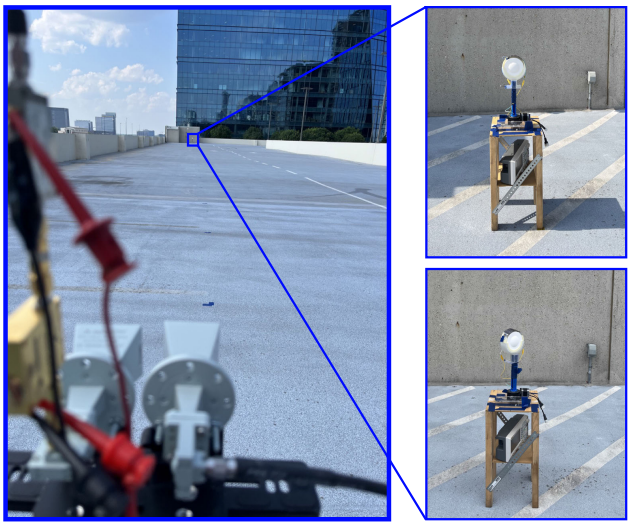

Fig. 11. Experimental setup of long-range ranging demonstration of the multi-lens mmID with incidence angles of 0° and 50° 82.5 m from the PoC FMCW radar.

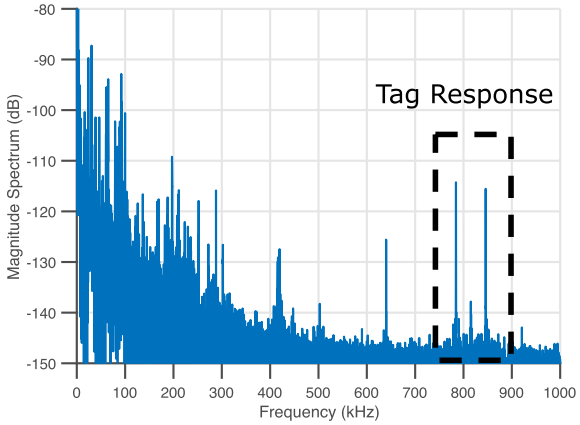

Fig. 12. Range-FFT magnitude spectrum of the proposed mmID at 40 m from PoC FMCW radar with mmID response labeled.

centered around the modulation frequency of the mmID with the separation being proportional to two times the f_b.

For the ranging estimation of the mmID, the two frequency components displayed in (7) contain the beat frequency, containing the ranging information of the mmID itself, are described by $f_{\text{mmID}_{\text{High}}} = f_{\text{Mod}} + f_b$ and $f_{\text{mmID}_{\text{Low}}} = f_{\text{Mod}} - f_b$. Limiting the two search windows based on the maximum range of 95 m, to allow for any additional timing delay as the received backscatter signal goes through the connecting cables in the receiver chain, results in a maximum f_b of 63.33 kHz from the modulation frequency of the mmID (817 kHz). Therefore, the resulting windowing functions $W_H(f)$ and $W_L(f)$ are described by

$$W_H(f) = \begin{cases} 1 & \text{if } f_{\text{Mod}} < f < (f_{\text{Mod}}) + 63.33 \text{ kHz} \\ 0 & \text{if o.w.} \end{cases}$$

$$W_L(f) = \begin{cases} 1 & \text{if } f_{\text{Mod}} - 63.33 \text{ kHz} < f < f_{\text{Mod}} \\ 0 & \text{if o.w.} \end{cases}$$

where f_{Mod} is the modulation frequency or the "ID" of the mmID. After windowing the range-FFT response, a peak detection algorithm was applied to both windows to select the $f_{\text{mmID}_{\text{High}}}$ and $f_{\text{mmID}_{\text{Low}}}$. The estimated range was then calculated using the expression

$$R_{\text{est}} = \frac{f_{\text{mmID}_{\text{High}}} - f_{\text{mmID}_{\text{Low}}}}{2} \left(\frac{T_c c}{2B} \right) \tag{8}$$

where $f_{\text{mmID}_{\text{High}}}$, $f_{\text{mmID}_{\text{Low}}}$, T_c, c, and B are the high modulation frequency peak in Hz, the low modulation frequency peak in Hz, the chirp period in seconds, the speed of light in m s^{-1}, and the bandwidth of the chirp signal in Hz. To calibrate the PoC ranging system, the mean of the 50 ranging estimates of the proposed mmID at 2.5 m is used as a reference measurement to calibrate out the time delay of the received backscattered response as it travels through the cables of the receiver chain. This mean is then subtracted from the subsequent measurements and the error of the true range estimates is then calculated. Fig. 13 displays the average error at each range step from the described ranging estimation confirming a highly accurate ranging of the mmID within 5 cm of the true value of range even at ultra-long ranges of 82.5 m from the radar. Thus, the system demonstrates the ultra-long-range operation for the use to be used in ultra-long-range localized sensing applications in digital twinning of complex urban and manufacturing environments. After displaying ranging with the best case link between the PoC FMCW radar and the multilens-based mmID, ranging the multilens-based mmID at the worst case angle of incidence of operation—at an angle of incidence of 50°—was also demonstrated. In this experiment, the multilens-based mmID was rotated so the angle of incidence from the PoC interrogator was 50° and an identical measurement as previously described was obtained with the results from this measurement displayed in Fig. 14. From this plot, the proposed cascaded lens topology maintained detectability and sufficient ranging accuracy (within 6 cm) even at highly oblique angles of 50°. When considering a multipath environment with numerous reflecting signals, as long as there is a line-of-sight link to the proposed mmID the response of the mmID will be detected based on the presented link budget analysis and accommodating for small-scale fading in the link margin. Furthermore, due to the cross-polarized design of the system, any environmental scattering will be reduced improving the resilience in cluttered environments. Lastly, due

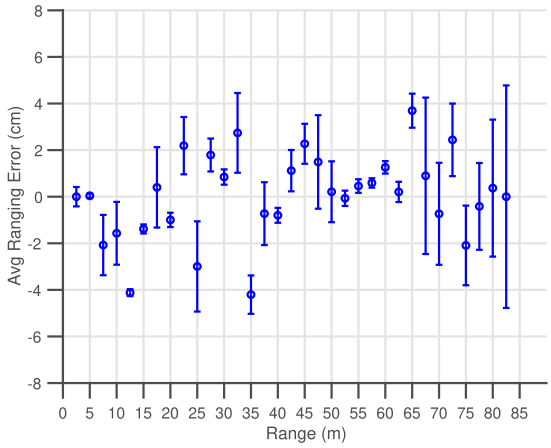

Fig. 13. Ranging error with standard deviation error bars of the multilens-based mmID for the best-case angle of incidence of 0°.

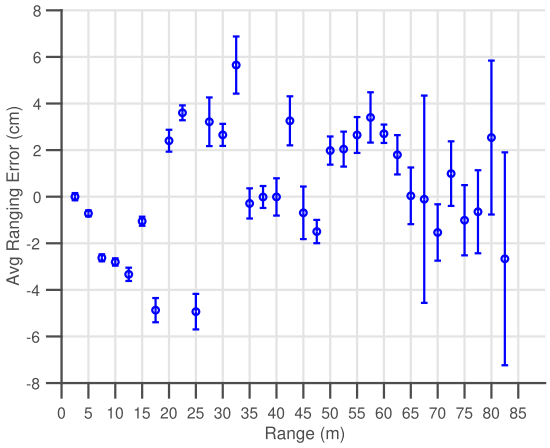

Fig. 14. Ranging error with standard deviation error bars of the multilens-based mmID for the worst case angle of incidence of 50°.

mmID modulating at f_{mod}, the mmID response is modulated away from the phase noise near the zero frequency range content allowing for more robust localization techniques to be used to further improve the ranging accuracy and detectability. Therefore, the proposed multilens-based mmID presents a highly orientation-agnostic energy autonomous sensor node for the expected highly complex links in "Smart" city environments.

V. Conclusion

In summary, the authors proposed for the first time, an energy autonomous, multilens-based mmID for the realization of future IoT swarms for digital twinning applications centered around 5G/mmWave infrastructure. By combining aspects of multi-lens optical system design and 5G/mmWave antenna design, a high-gain, wide-angle dielectric lens system was designed to provide angular coverage in both azimuth and elevation axes. A PoC prototype of the proposed multilens-based mmID presented a high differential RCS of -15.7 dBsm with a $\pm 50°$ -10 dB beamwidth resulting in an impressive 2.244 sr hemispherical coverage. The design presented an improved detectability compared to the single 3-D lens-based mmID counterpart while improving the solid angle coverage by over 204%. Furthermore, the mmID was integrated with a solar cell for energy autonomous operation enabling the massive scalability typically required for the creation of Digital Twinning "Smart" systems formed from IoT swarms. Using a PoC FMCW radar interrogator, the proposed mmID was then ranged accurately at ultra-long ranges up to 82.5 m with the mmID positioned at incidence angles of 0° and 50°; the best and worst case conditions of the mmID interrogation within the -10 db angular beamwidth. The mmID ranging system displayed a bounded ranging error of 6 cm within the true value even in the worst case conditions at ultra-long ranges. Thus, the proposed multilens-based mmID ranging system presents a unique opportunity for accurate localized sensing digital twinning applications even when deployed in highly complex wireless environments of "Smart" cities and "Smart" manufacturing. Additionally, the 3-D lens architecture of the design enables more freedom on the backscattering component with the potential to provide a reconfigurable steering through connecting the backscattering elements through a $N \times N$ low-power switching network. This effort sets the stage for further developments involving the integration of metalenses for the z-axis miniaturization of low-profile autonomous reconfigurable intelligent surfaces and smart-surface batteryless sensing systems for highly complex and rugged operational environments.

References

[1] S. Zhang, Y. Pu, Z. Wu, and Y. Luo, "A new K-band 1-bit broadband reconfigurable reflectarray antenna," in *Proc. 24th Int. Vac. Electron. Conf. (IVEC)*, Apr. 2023, pp. 1–2.

[2] L. Dai et al., "Reconfigurable intelligent surface-based wireless communications: Antenna design, prototyping, and experimental results," *IEEE Access*, vol. 8, pp. 45913–45923, 2020.

[3] E. Sharp and M. Diab, "Van Atta reflector array," *IRE Trans. Antennas Propag.*, vol. 8, no. 4, pp. 436–438, Jul. 1960.

[4] J. G. D. Hester and M. M. Tentzeris, "Inkjet-printed Van–Atta reflectarray sensors: A new paradigm for long-range chipless low cost ubiquitous smart skin sensors of the Internet of Things," in *IEEE MTT-S Int. Microw. Symp. Dig.*, May 2016, pp. 1–4.

[5] J. G. D. Hester and M. M. Tentzeris, "A mm-wave ultra-long-range energy-autonomous printed RFID-enabled Van–Atta wireless sensor: At the crossroads of 5G and IoT," in *IEEE MTT-S Int. Microw. Symp. Dig.*, Jun. 2017, pp. 1557–1560.

[6] A. Eid, J. G. D. Hester, and M. M. Tentzeris, "Rotman lens-based wide angular coverage and high-gain semipassive architecture for ultralong range mm-wave RFIDs," *IEEE Antennas Wireless Propag. Lett.*, vol. 19, no. 11, pp. 1943–1947, Nov. 2020.

[7] C. A. Lynch, A. O. Adeyeye, A. Eid, J. Hester, and M. M. Tentzeris, "Ultra-long-range dual Rotman lenses-based harmonic mmlD's for 5G/mm-wave loT applications," in *IEEE MTT-S Int. Microw. Symp. Dig.*, Jun. 2022, pp. 32–35.

[8] C. Lynch, A. O. Adeyeye, A. Eid, J. G. D. Hester, and M. M. Tentzeris, "5G/mm-wave fully-passive dual Rotman lens-based harmonic mmID for long range microlocalization over wide angular ranges," *IEEE Trans. Microw. Theory Techn.*, vol. 71, no. 1, pp. 330–338, Jan. 2023.

[9] J. Hasch, "Driving towards 2020: Automotive radar technology trends," in *IEEE MTT-S Int. Microw. Symp. Dig.*, Apr. 2015, pp. 1–4.

[10] E. Hayashi et al., "RadarNet: Efficient gesture recognition technique utilizing a miniature radar sensor," in *Proc. CHI Conf. Human Factors Comput. Syst.*, May 2021, pp. 1–14.

[11] A. O. Adeyeye, J. Hester, and M. M. Tentzeris, "Miniaturized millimeter wave RFID tag for spatial identification and localization in Internet of Things applications," in *Proc. 49th Eur. Microw. Conf. (EuMC)*, Oct. 2019, pp. 105–108.

[12] C. A. Lynch, A. O. Adeyeye, J. G. D. Hester, and M. M. Tentzeris, "When a single chip becomes the RFID reader: An ultra-low-cost 60 GHz reader and mmID system for ultra-accurate 2D microlocalization," in *Proc. IEEE Int. Conf. RFID (RFID)*, Apr. 2021, pp. 1–8.

[13] C. A. Lynch, G. Soto-Valle, J. Hester, and M. M. Tentzeris, "MmIDs enter the 3rd dimension: A camera inspired broadbeam high-gain retrodirective backscatter tag," in *IEEE MTT-S Int. Microw. Symp. Dig.*, Jun. 2023, pp. 1–4.

Charles A. Lynch, III (Student Member, IEEE) received the B.S. degree in electrical engineering from Rose-Hulman Institute of Technology, Terre Haute, IN, USA, in 2019. He is currently pursuing the M.S. and Ph.D. degrees in electrical engineering at the Georgia Institute of Technology, Atlanta, GA, USA.

He is currently a Research Assistant with the ATHENA Group, Georgia Institute of Technology. His current research interest focuses on the design, simulation, and fabrication of RF and millimeter-wave devices, specifically RFIDs and mmIDs and combining these low-power, wearable, ultralow-cost devices with radar for localized sensing in the Internet of Things systems.

Mr. Lynch received the audience choice in the 3MT Competition at the 2023 IEEE IMS conference.

Genaro Soto-Valle (Graduate Student Member, IEEE) received the B.S. degree in nanotechnology from the National Autonomous University of Mexico, Queretaro, Mexico, in 2020. He is currently pursuing the M.S. and Ph.D. degrees in electrical engineering at the Georgia Institute of Technology, Atlanta, GA, USA.

He is a Research Assistant with the ATHENA Group, Olympia, WA, USA. His research interests focus on additively manufactured RF systems for wireless environmental sensing and localization, particularly using mmWave modules targeted for the Internet of Things systems. More recently, he has been working on novel additive manufacturing techniques to enable micrometer-scale modules for sub-THz applications.

Jimmy G. D. Hester received the M.S. and Ph.D. degrees in electrical and computer engineering from the Georgia Institute of Technology, Atlanta, GA, USA, in 2014 and 2019, respectively.

He is currently the CTO and the Co-Founder of Atheraxon, Atlanta—the developers of the Theia mmWave localization technology—and an Adjunct Professor with the Department EECS, University of Michigan, Ann Arbor, MI, USA. His areas of expertise include backscatter communications, mm-wave antenna design, radar systems design, radar signal processing, digital communications, inkjet printing, and nanomaterials-based sensing.

Manos M. Tentzeris (Fellow, IEEE) received the Diploma degree (magna cum laude) in electrical and computer engineering from the National Technical University of Athens, Athens, Greece, and the M.S. and Ph.D. degrees in electrical engineering and computer science from the University of Michigan, Ann Arbor, MI, USA, in 1993 and 1998, respectively.

He was a Visiting Professor with the Technical University of Munich, Munich, Germany, in 2002; GTRI-Ireland, Athlone, Ireland, in 2009; LAAS-CNRS, Toulouse, France, in 2010; and a Humboldt Guest Professor with Florida Atlantic University (FAU), Nuremberg, Germany, in 2019. He is currently a Ken Byers Professor of flexible electronics with the School of Electrical and Computer Engineering, Georgia Institute of Technology, Atlanta, GA, USA, where he heads the ATHENA Research Group (20 researchers). He was the Head of the GT ECE Electromagnetics Technical Interest Group, the Georgia Electronic Design Center Associate Director of the RFID/Sensors Research, the Georgia Institute of Technology NSF-Packaging Research Center Associate Director of RF Research, and the RF Alliance Leader. He has helped develop academic programs in 3-D/inkjet-printed RF electronics and modules, flexible electronics, origami and morphing electromagnetics, highly integrated/multilayer packaging for RF, millimeter-wave, sub-THz and wireless applications using ceramic and organic flexible materials, paper-based RFID's and sensors, wireless sensors and biosensors, wearable electronics, "Green" and transient electronics, energy harvesting and wireless power transfer, nanotechnology applications in RF, microwave MEMs, and SOP-integrated (UWB, multiband, mmW, and conformal) antennas. He has authored more than 850 papers in refereed journals and conference proceedings, seven books, and 26 book chapters.

Dr. Tentzeris is a member of the URSI-Commission D, the MTT-15 Committee, and the Technical Chamber of Greece, an Associate Member of EuMA, and a Fellow of the Electromagnetic Academy. He was a recipient/co-recipient of the 2022 Georgia Tech Outstanding Doctoral Thesis Advisor Award, the 2021 IEEE Antennas and Propagation Symposium (APS) Best Student Paper Award, the 2019 Humboldt Research Prize, the 2017 Georgia Institute of Technology Outstanding Achievement in Research Program Development Award, the 2016 Bell Labs Award Competition 3rd Prize, the 2015 IET Microwaves, Antennas, and Propagation Premium Award, the 2014 Georgia Institute of Technology ECE Distinguished Faculty Achievement Award, the 2014 IEEE RFID-TA Best Student Paper Award, the 2013 IET Microwaves, Antennas and Propagation Premium Award, the 2012 FiDiPro Award in Finland, the iCMG Architecture Award of Excellence, the 2010 IEEE Antennas and Propagation Society Piergiorgio L. E. Uslenghi Letters Prize Paper Award, the 2011 International Workshop on Structural Health Monitoring Best Student Paper Award, the 2010 Georgia Institute of Technology Senior Faculty Outstanding Undergraduate Research Mentor Award, the 2009 IEEE TRANSACTIONS ON COMPONENTS AND PACKAGING TECHNOLOGIES Best Paper Award, the 2009 E. T. S. Walton Award from the Irish Science Foundation, the 2007 IEEE AP-S Symposium Best Student Paper Award, the 2007 IEEE MTT-S IMS Third Best Student Paper Award, the 2007 ISAP 2007 Poster Presentation Award, the 2006 IEEE MTT-S Outstanding Young Engineer Award, the 2006 Asia–Pacific Microwave Conference Award, the 2004 IEEE TRANSACTIONS ON ADVANCED PACKAGING Commendable Paper Award, the 2003 NASA Godfrey "Art" Anzic Collaborative Distinguished Publication Award, the 2003 IBC International Educator of the Year Award, the 2003 IEEE CPMT Outstanding Young Engineer Award, the 2002 International Conference on Microwave and Millimeter-Wave Technology Best Paper Award, Beijing, China, the 2002 Georgia Institute of Technology–ECE Outstanding Junior Faculty Award, the 2001 ACES Conference Best Paper Award, the 2000 NSF CAREER Award, and the 1997 Best Paper Award of the International Hybrid Microelectronics and Packaging Society. He was the General Co-Chair of the 2023 IEEE Wireless Power Transfer Technology Conference and Expo (WPTCE) in San Diego and the 2019 IEEE APS Symposium in Atlanta. He was the TPC Chair of the IEEE MTT-S IMS 2008 Symposium and the Chair of the 2005 IEEE CEM-TD Workshop. He is the Vice-Chair of the RF Technical Committee (TC16) of the IEEE CPMT Society. He is the Founder and the Chair of the RFID Technical Committee (TC24) of the IEEE MTT-S and the Secretary/Treasurer of the IEEE C-RFID. He has served as an Associate Editor for IEEE TRANSACTIONS ON MICROWAVE THEORY AND TECHNIQUES, IEEE TRANSACTIONS ON ADVANCED PACKAGING, and the *International Journal of Antennas and Propagation*. He has given more than 150 invited talks to various universities and companies all over the world. He is currently the IEEE EPS Distinguished Lecturer. He has served as one of the IEEE MTT-S Distinguished Microwave Lecturers and as one of the IEEE CRFID Distinguished Lecturers.